

# Growth Rates of Hydrogen Microbubbles in Reacting Femtoliter Droplets

Zhengxin Li, Hongbo Zeng, and Xuehua Zhang\*

*Department of Chemical and Materials Engineering, University of Alberta, Alberta T6G  
1H9, Canada*

E-mail: xuehua.zhang@ualberta.ca

## Abstract

Chemical reactions in small droplets are extensively explored to accelerate the discovery of new materials, increase efficiency and specificity in catalytic biphasic conversion and in high throughput analytic. In this work, we investigate the local rate of gas-evolution reaction within femtoliter droplets immobilized on a solid surface. The growth rate of hydrogen microbubbles ( $\geq 500$  nm in radius) produced from the reaction was measured online by high-resolution confocal microscopic images. The growth rate of bubbles was faster in smaller droplets, and of bubbles near the three-phase boundary in the same droplet. The results were consistent for both pure and binary reacting droplets and on substrates of different wettability. Our theoretical analysis based on diffusion, chemical reaction and bubble growth in a steady state predicted that the concentration of the reactant diffusing from the surrounding depended on the droplet size and the bubble location inside the droplet, in good agreement with experimental results. Our results reveal that the reaction rate may be spatially non-uniform in the reacting microdroplets. The findings may have implications for formulating chemical properties and uses of these droplets.

# Introduction

On-drop chemistry has been increasingly explored for fine chemical production based on biphasic reactions,<sup>1</sup> synthesis of novel bio- and nano-materials,<sup>2</sup> fast and sensitive chemical analysis,<sup>3</sup> and engineering chemorobotic platform.<sup>4-6</sup> Notably, many reactions confined in the droplets have been reported to be faster than on a large scale. The reaction rates may be enhanced by  $10^2$  to even  $10^6$  times compared to reactions in the bulk.<sup>7-9</sup> Droplet reactions may also simplify post purification processes for a wide range of biphasic reactions where reactants or products present in two immiscible fluid phases, such as oil and water or liquid and gas.<sup>10,11</sup> Microdroplet chemistry is considered to be green and sustainable, enabling efficient chemical conversion for a wide range of reactants under mild reaction conditions or without using metal, heat, or expensive catalyst.<sup>12</sup>

The fast chemical kinetics in small droplets is attributed to various interfacial phenomena,<sup>13</sup> including molecular configuration, local concentration or partial solvation of reactants, or unusual rate of electron transfer at the gas-water interface.<sup>14-18</sup> Electric potential energy localized at the interface may also alter the internal chemical equilibrium inside microdroplets.<sup>19</sup> Recently Zhong et al.<sup>20</sup> proposed that the surface of microdroplets may provide an energetically favourable environment for redox reactions in fast enzymatic protein digestion in microdroplet spray. In another case, reactant accumulation at the droplet surface was attributed to enhancement in the reaction between a droplet containing lipids and a droplet containing lipase.<sup>21</sup> The partial solvation of reactants at the interface may explain the accelerated reaction between microdroplets containing amines and  $CO_2$  where the reaction was only confined at the droplet surface.<sup>22</sup> The acceleration factor increases with the decrease in the concentration of the reactant.<sup>22</sup>

Beyond significant acceleration in reaction rate, microdroplet reaction enables the spontaneous occurrence of reactions that is thermodynamically unfavourable. The type of reactions ranges from oxidation of water in air to biomolecules or origin of life in prebiotic earth, for instance, the generation of hydroperoxide,<sup>23</sup> reduction of 2,6-dichlorophenolindophenol

(DCIP) by ascorbic acid in absence of catalyst,<sup>24</sup> and production of ribonucleotides from ribonucleosides.<sup>25</sup>

Higher chemical efficiency was reported not only for reacting droplets in the gas phase, but also for reactions between microdroplets and reactants dissolved in the surrounding liquid. An example is Mannich reaction in emulsion droplets.<sup>26</sup> A comprehensive analytic model was developed by Fallah-Araghi et al.<sup>26</sup> to explain the fast reaction rate of emulsion droplets. The reaction-adsorption mechanism took into account the reaction equilibrium constant and forward rate constant associated with the concentration difference of the reactants throughout the droplet. The mass flux between the droplets to the surrounding phase also plays an important role in the droplet reaction kinetics.<sup>27,28</sup> In this regard, femtoliter droplets immobilized on a solid surface have been used as a model system for the quantitative study of droplet reaction rates. As the three-phase contact line of surface droplets is pinned by the solid surface, these droplets are stable on the substrate as the reactant is supplied in a controlled flow.<sup>29-32</sup> The volume of surface droplets is conveniently controlled by the solvent exchange method.<sup>33-35</sup> The enhanced gas production rate in smaller surface droplets has been revealed recently from the growth rate of hydrogen nanobubbles as the product.<sup>36</sup> In particular, the bubble growth rates scaled with the droplet radius  $R$  with a power law  $R^{-n}$  with  $n$  from 0.7 to 2.4.

As chemical acceleration is mainly attributed to the important impact from physical and chemical properties of the interface, the enhancement may be expected to decay to a certain extent with the distance away from the droplet surface. A remaining question is whether the reaction rate inside the droplets is uniform spatially. In this work, we will focus on the local reaction rate inside femtoliter droplets. The growth rate of hydrogen bubbles from a gas-generating reaction in droplets will be followed by confocal microscopic imaging. In theoretical analysis of the local reaction rate, we take into account the reactant diffusion, chemical reaction equilibrium, and gas consumption by other bubbles coexisting in the droplet. To the best of our knowledge, our experimental results provide direct ev-

idence that the chemical kinetics and mass balance in the reacting microdroplets are not spatially uniform. These findings may help us to better understand the biphasic reaction kinetics of gas evolution reaction of microdroplets and to design and control droplet reaction in nanomaterials fabrication, heterogeneous catalysis, and in-demand hydrogen bubble production.

## Experimental

### Chemicals and materials

Methylhydrosiloxane (Sigma Aldrich) was the reactive liquid in the droplets. Octanol ( $\geq 95\%$ , Fisher Scientific) was the non-reactive liquid in a binary droplet. Sodium hydroxide (NaOH) ( $\geq 97\%$ , Alfa Aesar) acted as the catalyst for the gas-evolution reaction between siloxane droplets and water in the surrounding. All chemicals were used as received without any further purification. Water (18.2 M $\Omega$ cm) was purified by a Milli-Q purification unit (Millipore Sigma).

High precision cover glasses (60 mm length, 24 mm width, Azer Scientific) were hydrophobized with 3-aminopropyl triethoxysilane (APTES) ( $\geq 98\%$ , TCI America) and octadecyl trichlorosilane (OTS) ( $\geq 95\%$  Fisher Scientific) by following protocols in the literature.<sup>37–39</sup> Before use, hydrophobized glass substrates were sonicated in water and ethanol successively for 3 minutes and then dried in a stream of air. The surface tension of the droplet liquid  $\sigma_{liq-air}$  was tested with the drop shape analyzer (DSA-100, Kruss). The contact angle  $\theta$  of surface microdroplets on different substrates were constructed from 3D images collected from a scanning laser confocal microscope (Leica Stellaris 5) through 20 $\times$  objectives (0.60 NA). Table 1 and 2 list relevant physical properties of droplet liquids and contact angle of surface droplets  $\theta$  on various types of the substrates. Droplet formation and chemical reactions were conducted at the room temperature of  $\sim 21^\circ\text{C}$ .

Table 1: Physical properties of liquids used in droplet formation

Liquid (vol)	$\sigma_{liq-air}$ (mNm <sup>-1</sup> )	Viscosity $\mu$ (mPa·s)
Water	69	1
Siloxane	19	15 ~ 30
Octanol	21	9

Table 2: Contact angle of femtoliter droplets on the substrates used in our experiments

Droplet liquid	Substrate	$\theta$ (°)
Siloxane	1	~ 26(±6)
Siloxane	2	~ 31(±5)
Siloxane	3	~ 68(±9)
Siloxane + Octanol	3	~ 32(±7)
Siloxane + Octanol	4	~ 23(±5)

## Formation of surface microdroplets of reactive liquid

Surface microdroplets were prepared within a well reactor as sketched in Figure 1A. The well reactor consisted of a piece of the glass substrate and a silicone rubber spacer. The well was 14 mm in both length and width, and 3 mm in depth. Surface microdroplets were formed by the standard solvent exchange process where the solution of droplet liquid (Solution A) was displaced by a poor solvent for droplet liquid (Solution B). In our experiments, Solution A was 1 vol% siloxane in acetone ( $\geq 99.5\%$ , Fisher Scientific). Solution B was water.

During the solvent exchange, the well was initially filled with 200  $\mu$ l of Solution A. Then a micropipette was used to add 200  $\mu$ l of solution B into the well at a rate of 2 drops per 10 s. Then 200  $\mu$ l of the liquid was removed from the well by a micropipette at the same rate. Addition of Solution B into the well-induced formation and growth of surface microdroplets on the substrate, as sketched in Figure 1B. The process of addition-removal of solution B was repeated 4 times till the liquid in the well became clear and surface microdroplets formed on the wall. At the completion of the solvent exchange, the liquid in the well was not pure water, but an aqueous solution with a volume of 400  $\mu$ l contained acetone of  $> 6\%$ , v/v. The presence of acetone in the surrounding phase was determined by a microvolume ultraviolet-visible (UV-Vis) spectrophotometer (Nanodrop 2000c, Thermo Fisher). Figure

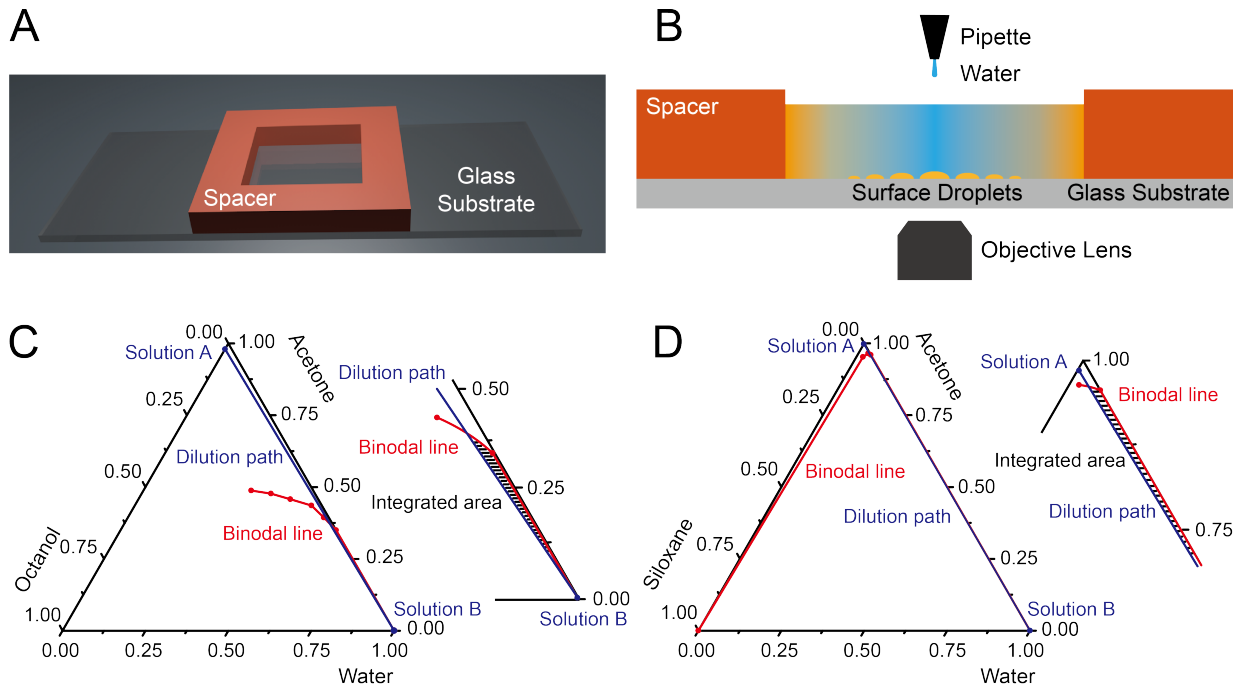


Figure 1: (A) The sketch of the well reactor used in our experiments for formation and reaction of droplets. (B) Illustration of preparing surface microdroplets by solvent exchange. (C)&(D) Ternary phase diagrams of (A) Siloxane-acetone-water system and (B) Octanol-acetone-water system. Points labelled as solution A&B are respectively the composition points of solution A&B. Black shaded areas surrounded by binodal lines (red) and dilution paths (blue) represent the oversaturation of each component in the mixing front.

S1 in supporting materials demonstrates the UV-Vis absorption spectrum of a sample from the surrounding phase with  $\sim 9\%$  (v/v) acetone.

## **Formation of surface microdroplets of reactive and non-reactive liquids**

Binary droplets consisting of octanol and siloxane were prepared on both APTES-coated and OTS-coated substrates. Solution A was 2 vol% octanol and 0.3 vol% siloxane in acetone solution. A trace amount of fluorescence dye rhodamine 6G (R6G,  $\sim 5 \mu\text{M}$ ) was added into Solution A for visualization by confocal imaging. Solution B was water. The solvent exchange was performed in the well reactor by following the same procedure as above to form binary droplets on the substrate. By the end of the solvent exchange, the concentration of acetone in the solution inside the well was around 6% (v/v), and the volume of the solution was controlled to be at 400  $\mu\text{l}$ .

The composition of binary droplets was predetermined by the oversaturation level of octanol and siloxane during the solvent exchange,<sup>40</sup> which could be approximately estimated according to the difference of dilution path and the binodal curve in the solubility phase diagram. The detailed protocol and the analysis were reported in literature.<sup>40,41</sup> Ternary phase diagrams of octanol-acetone-water and siloxane-acetone-water were prepared by titration and demonstrated in Figure 1C&D. The area surrounded by binodal curves and dilution path in the ternary phase diagram represents the overall oversaturation (octanol:siloxane  $\sim 4:1$ ).

## **Tracking microbubbles in reacting droplets**

50  $\mu\text{l}$  of 0.24 M NaOH aqueous solution was added into the well by a micropipette to trigger the reaction between siloxane and water. The existence of acetone was confirmed to be necessary for the bubble formation by controlled experiments, in which acetone was almost

removed by repeating adding water and removing the mixture from the well 12 times.

Laser scanning confocal microscopes (Leica SP5 and Leica Stellaris 5) through  $100\times$  objectives (1.44 NA/1.49 NA) were employed to track the reaction process in-situ. Bright-field images and confocal images of the bubble formation process were respectively recorded with a transmission detector and a hybrid detector. 488/534 nm laser beams were used to excite the dye R6G incorporated in droplets. The pixel sizes of the videos range from 151 nm to 303 nm. The frame rate was 0.77 fps.

Open source PIMS, scikit, and trackPy package for python, combined with ImageJ, were applied to analyze the images. Droplets and bubbles in the field of view were processed frame by frame by home-built python code. The base areas of hydrogen bubble  $a_b$  and reacting droplet  $A_b$  were extracted as a function of time  $t$ . Time zero ( $t_0$ ) was defined as the moment when NaOH solution was added to the well. Distance from the center of the bubble base to the three-phase contact line of the droplet  $D_b$  was measured by ImageJ. In most experiments, droplets and bubbles on our homogeneous substrates were assumed to keep the shape of a spherical cap without the strong pinning effect. Some bubbles in small droplets ( $R_b < 5 \mu\text{m}$ ) grew irregularly and were not considered when calculating the average growth rate of hydrogen bubbles.

## Results and discussion

### Theoretical model: Local reaction rate in microdroplets

The chemical reaction of siloxane dehydrocoupling is catalyzed by hydroxide from the aqueous phase (Figure 2). At first, hydroxide in bulk attacks silicon atoms of siloxane. Then, hydroxide is reformed by consuming water, and hydrogen is liberated. The oversaturation of the hydrogen product inside the reacting droplet leads to the formation and growth of multiple hydrogen bubbles.

The dimensions of a bubble and a reacting droplet are sketched in Figure 2B. Base radius

of bubble  $r$  and droplet  $R_b$  were calculated from the base area of bubble  $a_b$  and droplet  $A_b$  as  $r = (a_b/\pi)^{0.5}$  and  $R_b = (A_b/\pi)^{0.5}$ . The radius of curvature  $R_s$  of the droplet was calculated as  $R_s = R_b/\sin\theta$ . Based on the contact angle of the droplet  $\theta$ , the base radius  $R_b$ , the curvature radius  $R_s$ , and the distance from the bubble center to the droplet rim  $D_b$ , the shortest distance from the bubble center to the droplet surface  $D_s$  can also be calculated by the following equation:

$$D_s = R_s - \sqrt{(R_b - D_b)^2 + R_b^2/\tan^2\theta}. \quad (1)$$

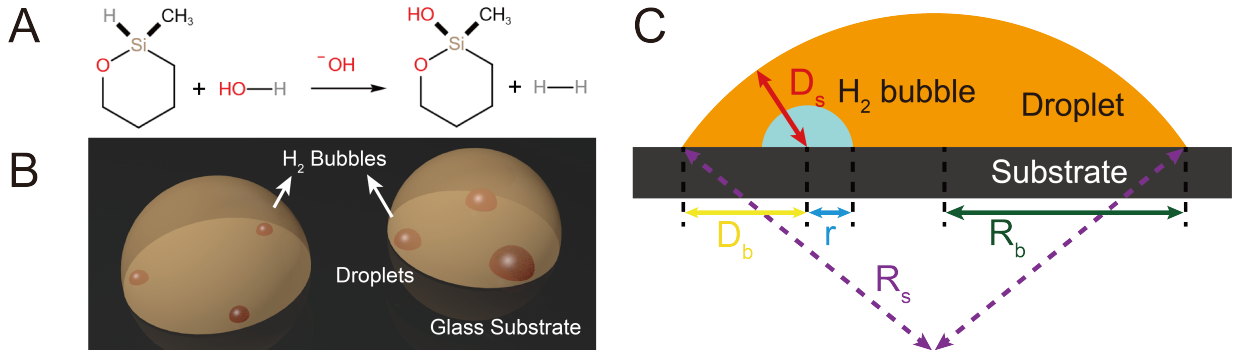


Figure 2: (A) The chemical equation of siloxane dehydrocoupling with water. (B) Illustration of hydrogen bubbles formed in droplets. (C) Base radius of droplet  $R_b$  (green) and bubble  $r$  (blue), radius of the curvature  $R_s$ , distance from the bubble center to the droplet rim  $D_b$  (yellow) and the droplet surface  $D_s$  (red) in the sketch of a surface microdroplet.

The reaction in our experiments is irreversible. The rate-limiting step in local gas production in the droplet is water (the reactant) diffusion into the droplets, a step that determines the location and the rate of the bubbles. Hydrogen produced from the reaction located at the droplet will be discussed in a later section. The reaction with siloxane consumed water and reduced the water concentration in the droplet. The mass balance of water in the droplet consists of the water diffusion and the chemical reaction. In a spherical droplet, the water concentration profile will be analyzed in the radial direction. The mass balances of water inside the droplet can be given by Fick's law:

$$\partial_t C_w(D_s) = D\nabla^2 C_w(D_s) - k_r C_w(D_s) C_{SiH}. \quad (2)$$

$\partial_t$  is the time derivative.  $\nabla$  is the Nabla operator.  $D$  is the diffusion coefficient of the hydrogen in and out of the droplet.  $C_w(D_s)$  is the local concentration of water with the distance  $D_s$  from the droplet surface.  $C_{SiH}$  is the concentrations of siloxane, which can be taken as a constant in the droplet.  $k_r$  is the rate constant of the reaction. At the point with distance  $D_s$  from the droplet surface, the variation of water concentration  $\partial_t C_w(D_s)$  is given by the water diffusion  $D\nabla^2 C_w(D_s)$  minus the water consumption by the chemical reaction  $k_r C_w(D_s) C_{SiH}$ .

Assuming the steady state that water concentration inside the droplet was constant with time,  $\partial_t C_w(D_s)$  was zero and can be neglected in equation 2:

$$k_r C_w(D_s) C_{SiH} = D\nabla^2 C_w(D_s). \quad (3)$$

We defined a characteristic diffusion length  $\epsilon$  as  $\sqrt{D/(k_r C_{SiH})}$  to describe the competing effect from water diffusion from the droplet surface and from water consumption by the chemical reaction in the droplet.<sup>26</sup> Solving equation 3 (see Supporting Materials for the derivation), we get:

$$C_w(D_s) = C_w(D_s)|_{D_s=0} \frac{R_s \sinh(R_s - D_s)/\epsilon}{(R_s - D_s) \sinh R_s/\epsilon}. \quad (4)$$

Based on equation 4, water concentration at a distance  $D_s$  to the droplet surface  $C_w(D_s)$  is determined by the water concentration nearing the droplet surface  $C_w(D_s)|_{D_s=0}$ , radius of the droplet curvature  $R_s$ , and diffusion length  $\epsilon$ . From the profile of  $C_w(D_s)$  in equation 4, the profile of production rate of hydrogen  $\dot{m}(D_s)$  throughout the droplet can be given by  $\dot{m}(D_s) = k_r C_{SiH} C_w(D_s)$ , as:

$$\begin{aligned} \dot{m}(D_s) &= k_r C_{SiH} C_w(D_s)|_{D_s=0} \frac{R_s \sinh(R_s - D_s)/\epsilon}{(R_s - D_s) \sinh R_s/\epsilon} \\ &= \dot{m}(D_s)|_{D_s=0} \frac{R_s \sinh(R_s - D_s)/\epsilon}{(R_s - D_s) \sinh R_s/\epsilon}. \end{aligned} \quad (5)$$

$\dot{m}(D_s)|_{D_s=0}$  is the theoretical hydrogen production rate nearing the droplet surface.

In the above analysis, the profile of hydrogen production rate is obtained along the radial direction inside a spherical droplet. In surface droplets with contact angles much lower than  $90^\circ$ , microbubbles on the substrate are close to the droplet surface than to the center of the sphere. Hence the radial concentration profile from equation 5 services a good approximation for the hydrogen supply for microbubbles over the base area of the droplet. Assuming a balanced state that the hydrogen product surrounding the bubble diffuses to the bubble surface and is consumed by the bubble growth, the average bubble growth rate  $\dot{r}(D_s)$  should be approximately proportional to  $\dot{m}(D_s)$  in equation 5 and can be fit by the same profile:

$$\dot{r}(D_s) = \dot{r}(D_s)|_{D_s=0} \frac{R_s \sinh(R_s - D_s)/\epsilon}{(R_s - D_s) \sinh R_s/\epsilon}. \quad (6)$$

$\dot{r}(D_s)|_{D_s=0}$  is the theoretical average growth rate of the hydrogen bubble nearing the droplet surface.

## Growing microbubbles in reacting surface droplet

The contact angle of the reacting droplets constructed from 3D confocal images were respectively  $\sim 26^\circ(\pm 6^\circ)$  (Figure 3A&B) and  $\sim 31^\circ(\pm 5^\circ)$  (Figure 3D-F). After introducing NaOH solution into the reactor, microbubbles nucleate throughout reacting droplets. The radius of microbubbles ranges from a few hundred nanometers to several microns. Screenshots in Figure 3A&B show the continuous growth of bubbles inside two large droplets with the base radius  $R_b$  of  $9.8 \mu\text{m}$  and  $7.5 \mu\text{m}$ . Figure 3D-E show hydrogen bubbles grow in small droplets with  $R_b$  less than  $4 \mu\text{m}$ . The number of bubbles is much higher in a larger droplet.

As bubbles grew with time, more of the droplet base area was taken up by bubbles. Two adjacent bubbles may coalesce and merge into a larger bubble. The elliptical morphology of bubbles after coalescence suggests that bubbles are pinned by the substrate due to the slow relaxation in the viscose droplet. For large bubbles with the base radius  $r$  larger than  $2 \mu\text{m}$

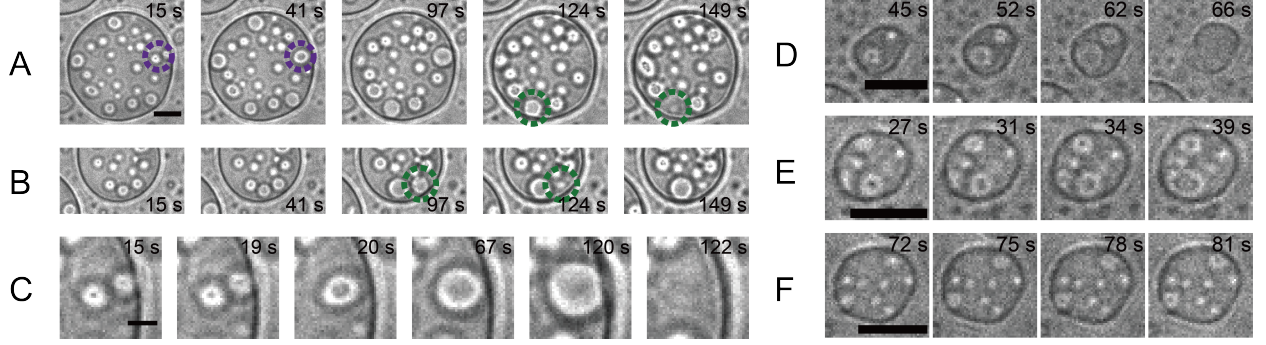


Figure 3: (A)&(B) Screenshots of hydrogen bubbles in siloxane droplets with the base radius of  $9.8 \mu\text{m}$  (A) and  $7.5 \mu\text{m}$  (B). Purple circles and green circles denote where bubbles coalesce and collapse. (C) Zoom-in of two bubbles in (A) from coalescence to detachment. (D)-(E) Screenshots of hydrogen bubbles in droplets with the base radius of  $1.8 \mu\text{m}$  (A),  $2.2 \mu\text{m}$  (B), and  $2.8 \mu\text{m}$  (C). The length of scale bars in (A)(B)(D)(E) are  $5 \mu\text{m}$ , and in (C) is  $2 \mu\text{m}$ .

near the droplet rim, they may collapse and detach from the substrate. Figure 3C enlarges two representative bubbles in Figure 3A from coalescence to detachment. The collapse of the bubble near the rim may be due to the rupture of the oil thin film between the bubble and the aqueous phase outside the droplet.<sup>36</sup> More quantitative study of bubble coalescence and bubble detachment on the solid surface was reported in previous work.<sup>42</sup>

For multiple bubbles in a droplet, bubbles around the droplet rim grew faster than those near the droplet center. For example, from  $t = 15 \text{ s}$  to  $t = 97 \text{ s}$  in Figure 3A&B, bubbles at the droplet rim became  $\sim 40\%$  larger in base radius, while bubbles far from the droplet rim remained almost the same size. In Figure 4A&B, the base radius of bubbles  $r$  was plotted as the function of  $t$ . We approximate that bubbles grew linearly and calculate the average growth rate of each bubble by linear fitting. The distance from the bubble center to the droplet surface  $D_s$  was also calculated by equation 1. Figure 4C&D show that the bubble growth rate decreases with the increase in  $D_s$ . The experimental data can be well fitted with the theoretic model.

On the APTES-Si substrate where the contact angle of droplets was  $\sim 31^\circ(\pm 5^\circ)$ , bubbles in seven small droplets with  $R_b$  ranging from  $1.8 \mu\text{m}$  to  $4.0 \mu\text{m}$  were followed with time. The average growth rates of bubbles were approximately calculated by linear fitting, and plotted

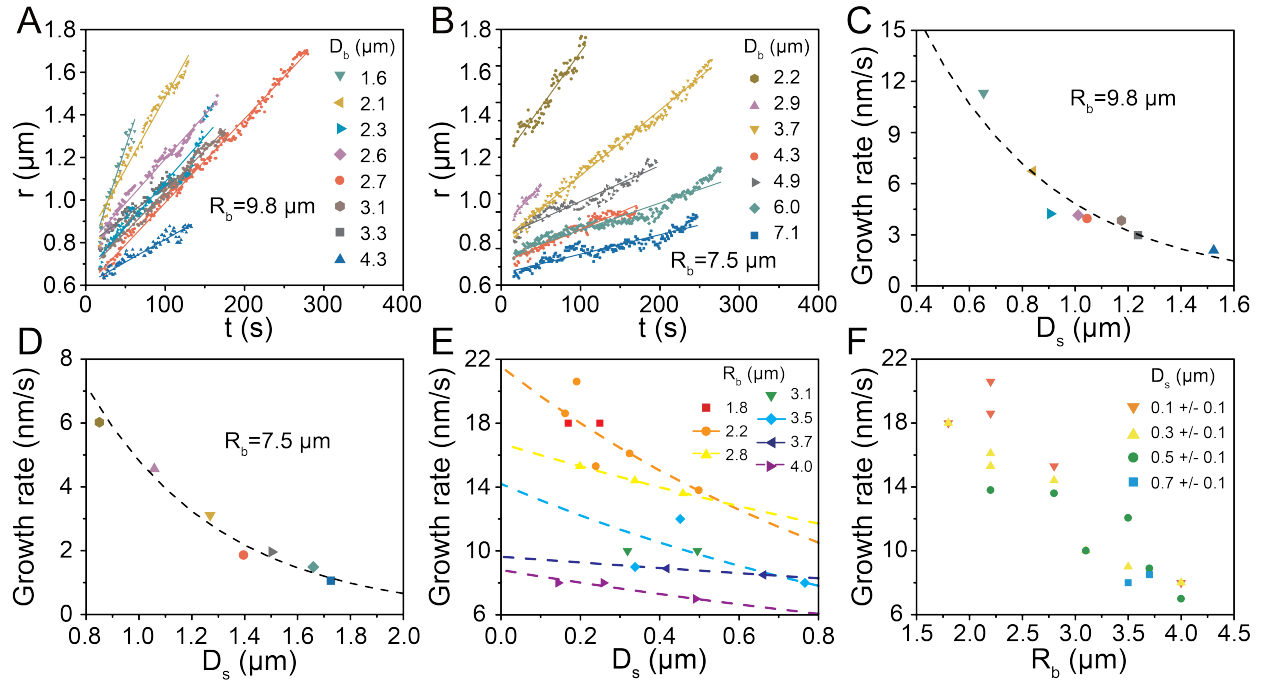


Figure 4: (A)&(B) Base radius  $r$  of hydrogen bubbles from Figure 3A&B as a function of time. (C)&(D) The average growth rate of hydrogen bubbles in (A)&(B) as a function of the distance from the droplet surface to the bubble center  $D_s$ . Dashed lines in (C)-(E) are from the fitting of equation 6. (E) The average growth rate of hydrogen bubbles as a function of the distance from the bubble to the droplet surface  $D_s$ . Bubbles in (E)&(F) are from droplets with the base radius  $R_b$  ranging from 1.8  $\mu\text{m}$  to 4.0  $\mu\text{m}$ . (F) The average growth rate of hydrogen bubbles as a function of the base radius of the droplet  $R_b$ .

as a function of  $D_s$  in Figure 4E. Overall the influence from  $D_s$  in small droplets was relatively trivial. Figure 4F shows that the growth rate of bubbles increased with the decrease in the droplet size.

Table 3 summarize the parameters  $\epsilon$  and  $\dot{r}(D_s)|_{D_s=0}$  in the theoretical fittings plotted in Figure 4C-E.  $\dot{r}(D_s)|_{D_s=0}$  is higher in smaller droplets, consistent with the faster growth rate of bubbles in smaller droplets in the same group of experiments. The enhanced reaction rate in smaller droplets was also found and quantitatively analyzed in our previous results.<sup>28,36</sup> The accelerated bubble kinetics in smaller droplets was attributed to the faster accumulation of the hydrogen product in smaller droplets with a higher surface-to-volume ratio.

Table 3: Fitting parameters  $\epsilon$  and  $\dot{r}(D_s)|_{D_s=0}$  for experimental results from siloxane droplets in Figure 4.  $R_b$  and  $R_s$  are the base radius and curvature radius of the droplet.  $\theta$  is the contact angle of the droplet.  $D$ ,  $k_r$ , and  $C_{SiH}$  are the hydrogen diffusion coefficient in the droplet, rate constant of the reaction, and siloxane concentration in the droplet.

$R_b/R_s$ ( $\mu\text{m}$ )	$\theta$ ( $^\circ$ )	$\epsilon = \sqrt{D/(k_r C_{SiH})}$ ( $\mu\text{m}$ )	$\dot{r}(D_s) _{D_s=0}$ (nm/s)
9.8/22.4	$\sim 26^\circ \pm 6^\circ$	0.5	34
7.5/17.1	$\sim 26^\circ \pm 6^\circ$	0.5	36
4.0/6.1	$\sim 31^\circ \pm 5^\circ$	1.7	9
3.7/5.6	$\sim 31^\circ \pm 5^\circ$	3.4	10
3.5/5.3	$\sim 31^\circ \pm 5^\circ$	1.2	14
2.8/4.3	$\sim 31^\circ \pm 5^\circ$	1.8	17
2.2/3.4	$\sim 31^\circ \pm 5^\circ$	1.0	22

## Effects from the contact angle of the reacting droplet

Both surface coating and the liquid composition in the droplet were varied to provide three different contact angles in our experiments from  $23^\circ$  to  $68^\circ$ . On an APTES-Si substrate where siloxane droplets were produced with the contact angle of  $\sim 68^\circ(\pm 9^\circ)$ , bubbles were found to exclusively nucleate at the droplet rim. As shown in Figure 5A, a necklace of microbubbles developed around the rim of the droplet in contact with the basic solution. For small droplets with the base radius  $R_b$  less than  $2 \mu\text{m}$ , as in Figure 5B, only one or two bubbles in most cases can be accommodated in a droplet. Screenshots in Figure 5C demonstrates the evolution of bubbles in a representative droplet with  $R_b =$  of  $12.3 \mu\text{m}$ .

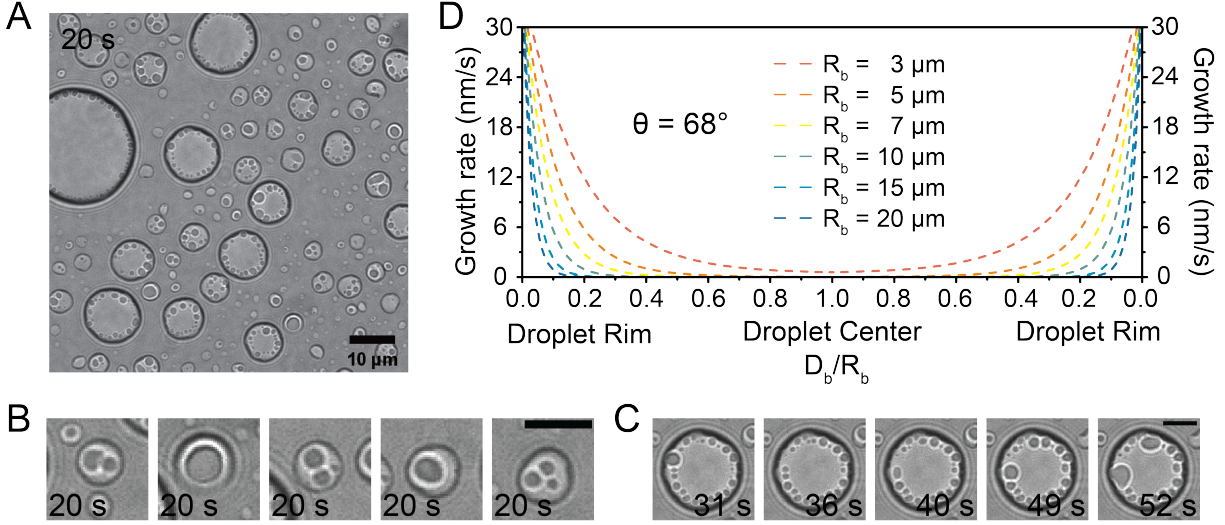


Figure 5: (A) Hydrogen bubbles in siloxane droplets with the contact angle of  $68^\circ(\pm 9^\circ)$ . (B) Zoom-in of small droplets ( $R_b < 3 \mu\text{m}$ ) from (A). (C) Screenshots of hydrogen bubbles grow in a siloxane droplet with the base radius of  $12.3 \mu\text{m}$ . Scale bars in (B)&(C) were  $5 \mu\text{m}$ . (D) Theoretical average growth rate profile of hydrogen bubbles crossing the droplet base. The contact angle  $\theta$  was taken as  $68^\circ$ .  $\epsilon$  and  $\dot{m}(D_s)|_{D_s=0}$  were taken as  $0.5 \mu\text{m}$  and  $34 \text{ nm/s}$ , same the fitting parameters in Figure 4C.

From equations 1&6,  $\dot{r}(D_s)$  was approximately estimated as a function of normalized distance to the droplet rim  $D_b/R_b$  crossing the droplet base, as shown in Figure 5D. The contact angle of droplets was taken as  $68^\circ$ .  $\epsilon$  and  $\dot{r}(D_s)|_{D_s=0}$  were set as  $0.5 \mu\text{m}$  and  $34 \text{ nm/s}$ , same as the fitting parameters in Figure 4C. Apart from droplet with  $R_b$  of  $3 \mu\text{m}$ ,  $\dot{r}(D_s)$  rapidly decrease below  $1 \text{ nm/s}$  before reaching the droplet center. Taking a droplet with the base radius  $R_b$  of  $10 \mu\text{m}$  as the example,  $\dot{r}(D_s)$  already decreased to  $0.14 \text{ nm/s}$  at  $D_b/R_b$  of  $0.3$ , suggesting an extremely low water concentration and slow reaction rate at  $D_b = 3 \mu\text{m}$ . It may take a long time for hydrogen to reach the concentration level for bubbles to nucleate at such a slow reaction rate. The rapid decrease in water concentration inside droplets with high contact angles explains why bubbles only nucleate and grow at the droplet rim.

Screenshots in Figure 6A&B demonstrate the bubble growth in binary droplets on two substrates. The contact angle of binary droplets were  $32^\circ(\pm 7^\circ)$  on the OTS-Si substrates and  $\sim 23^\circ(\pm 5^\circ)$  on the APTES-Si substrates.  $R_b$  of the binary droplets were  $22 \mu\text{m}$  and  $9.0 \mu\text{m}$ . Similar to bubbles in pure droplets shown in Figure 3, bubbles nucleated and grew

throughout binary droplets. Figure 6C&D respectively demonstrate hydrogen bubbles close to the droplet rim and at the droplet center. The lifetime for a bubble at the droplet rim is usually less than 10 seconds from nucleation to detachment, much shorter than that of inner bubbles. Figure 6E&F present sizes of several representative bubbles with different  $D_b$  to the droplet rim. Bubbles at the droplet rim grow much faster than bubbles at the droplet center.

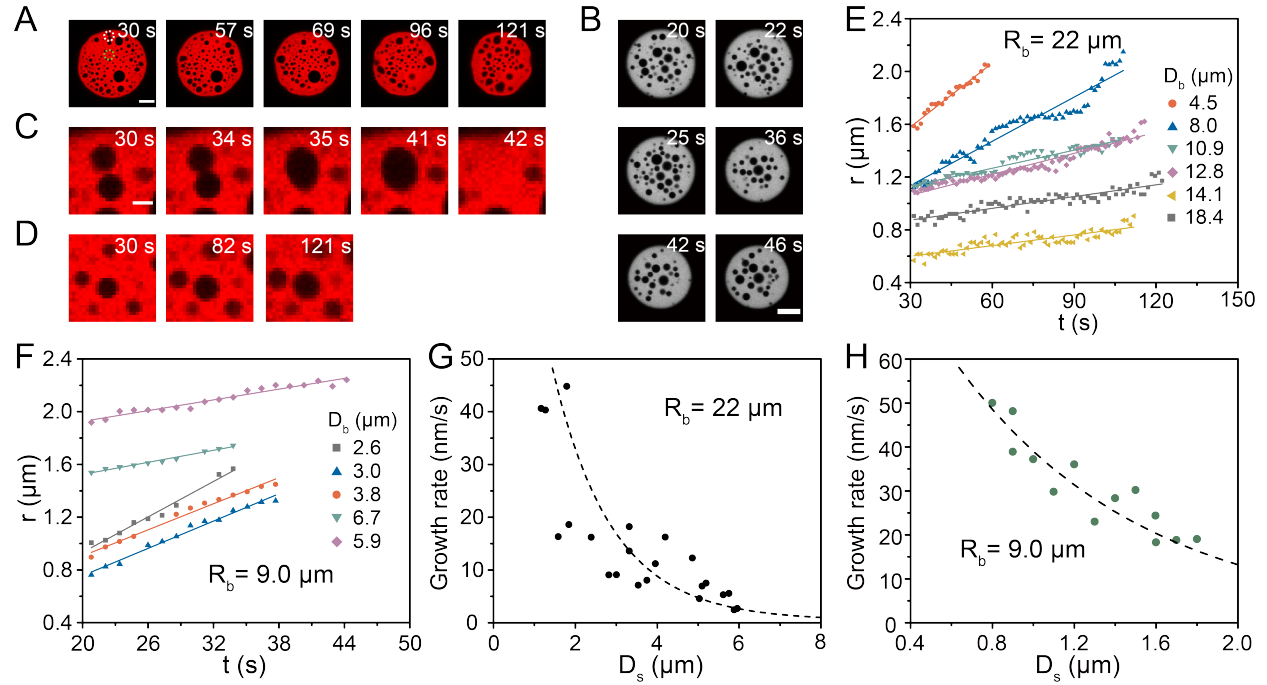


Figure 6: (A)&(B) Bubbles grow in a binary droplet on an APTES-Si substrate (A) and an OTS-Si substrate (B). The base radius of the droplet  $R_b$  are  $22 \mu\text{m}$  in (A) and  $9.0 \mu\text{m}$  in (B). The contact angle of binary droplets on the substrate were (A)  $\sim 32^\circ(\pm 7^\circ)$  and (B)  $\sim 23^\circ(\pm 5^\circ)$ . The scale bars are (A)  $10 \mu\text{m}$  and (B)  $5 \mu\text{m}$ . (C)&(D) Zoom-in images of hydrogen bubbles at the droplet rim (C) and the droplet center (D). (C)&(D) are taken from the white and green circle in (A). The scale bar for (C)&(D) in (C) was  $2 \mu\text{m}$ . (E)&(F) Base radius  $r$  of several representative hydrogen bubbles from (A)&(B) as a function of time. (G)&(H) Average growth rate of hydrogen bubbles from (A)&(B) as a function of distance to the droplet surface  $D_s$ . Dashed lines in (G)&(H) are from the fitting of equation 6.

Average growth rates of bubbles are plotted as a function of  $D_s$  in Figure 6G&H. Although data points were scattered in binary droplets, the overall trend was that there was a strong dependence of growth rate on  $D_s$ . On the other hand, even the siloxane concentration in binary droplets was lower, the growth rate of bubbles near the droplet rim can go up to

$\sim 50$  nm/s, much faster than bubble growth in pure siloxane droplets. As a result, both bubble coalescence and bubble detachment were more frequent in binary droplets than in pure droplets.

Dashed lines in Figure 6G&H are the fittings of experimental results by our theoretic model. Table 4 summarize the fitting parameters  $\epsilon$  and  $\dot{r}(D_s)|_{D_s=0}$  of binary droplets. Corresponding to experimental results that bubble kinetics in binary droplets was faster than in pure droplets,  $\dot{r}(D_s)|_{D_s=0}$  was also found to be higher than that of pure droplets. The accelerated bubble kinetics in binary droplets was probably from the increased water solubility with the addition of polar octanol into the droplets. Higher water concentration in the droplet contributes to a faster chemical reaction rate.

Table 4: Fitting parameters  $\epsilon$  and  $\dot{r}(D_s)|_{D_s=0}$  for experimental results from octanol-siloxane binary droplets.  $R_b$  and  $R_s$  are the base radius and curvature radius of the droplet.  $\theta$  is the contact angle of the droplet.  $D$ ,  $k_r$ , and  $C_{SiH}$  are the hydrogen diffusion coefficient in the droplet, rate constant of the reaction, and siloxane concentration in the droplet.

$R_b/R_s$ ( $\mu\text{m}$ )	$\theta$ ( $^\circ$ )	$\epsilon = \sqrt{D/(k_r C_{SiH})}$ ( $\mu\text{m}$ )	$\dot{r}(D_s) _{D_s=0}$ (nm/s)
22.0/41.5	$\sim 32^\circ \pm 7^\circ$	1.2	143
9.0/23.0	$\sim 23^\circ \pm 5^\circ$	0.8	137
7.4/18.9	$\sim 23^\circ \pm 5^\circ$	0.9	154

## Further discussion: On-droplet and in-droplet hydrogen production

The reaction in our experiments can certainly take place on the surface of the droplets, due to abundant siloxane, water and the catalyst in the surrounding. On-droplet hydrogen is expected to be limited in amount. Moreover, the molecules at the interface may react even more readily to react.<sup>7-9,13</sup> Many reactions that almost do not happen when reactants are located in immiscible phases can occur at the interface. However, the number of interfacial molecules is at least 2 orders of magnitudes less than the number of molecules inside a droplet with a typical size in our experiments. Although the production rate of hydrogen from the interfacial reaction is expected to be faster thanks to the faster reaction rate, the low number of interfacial molecules at any given time limits the total amount of gas production. As the

diffusion coefficient of hydrogen in organic liquid (droplet phase) is much faster than in water and the small dimension of the droplets (especially in the height), hydrogen produced at the droplets may reach a certain constant concentration in the droplet at equilibrium with hydrogen dissolved in the surrounding in a short time.

In addition to hydrogen from on-droplet production, the in-droplet production of hydrogen analyzed in our model is attributed to water (carrying the catalyst) diffusing into the droplets. In-droplet water reacts with siloxane to produce hydrogen locally in the droplets. We note that the presence of co-solvent acetone in the system can increase the solubility of water in the droplets and enhance in-droplet hydrogen concentration from the reaction inside the droplets. To a certain extent, even for pure siloxane droplets in absence of acetone, it may be impossible to fully eliminate diffusion of water into reactive droplets as the droplet surface is not impermeable.

A final note is that in-droplet reaction may drive continuous intake of water into droplets, in contrast to the equilibrium from the pure partition where the intake of water is limited by the solubility of water in droplet liquid. The reason is that free water is chemically converted in fast in-droplet reactions, compared to the slow mass transfer of water. The concentration of water may not reach the solubility limit in the droplet. The mechanism is similar to what was reported in the latest work on acid-base reactions, and is the reason why the droplet sensing can achieve very high sensitivity.<sup>43,44</sup>

## Conclusion

In summary, the growth rate of hydrogen microbubbles as the gas product was quantified to report the reaction rate inside the microdroplet. The dependence of bubble growth rate on the location inside the droplets, and on the size, morphology and composition of the droplets all suggest that the reaction rate inside microdroplets may be spatially non-uniform. In our theoretical analysis, diffusion of reactant (water) into the droplets is considered to be the

rate-limiting step in bubble growth. The predicated local gas concentration is in good agreement with the effects from droplet size, substrate wettability and the composition of binary droplets.

Understandings of in-droplet bubble formation may lay a foundation for exploring droplet reactions with enhanced chemical kinetics and hydrogen generation. Moreover, nanobubbles encapsulated in surface droplets may lead to a new pathway to functional slippery surfaces to reduce the surface friction,<sup>45</sup> porous surface-bound materials by templating nanobubbles,<sup>46</sup> or coated bubbles used in biomedical imaging, and therapeutic delivery of oxygen or other pharmaceutical compounds.<sup>47,48</sup>

### List of symbols

<b>Symbols</b>	<b>Definition</b>
$\sigma_{liq-air}$	Interfacial tension between liquid and air
$\mu$	Viscosity
$\theta$	Contact angle of surface microdroplet on the solid substrate
$A_b$	Base area of surface microdroplet
$a_b$	Base area of surface microbubble
$t$	Time calibrated by adding NaOH solution
$R_b$	Base radius of surface microdroplet
$R_s$	Radius of the curvature (spherical model)
$r$	Base radius of surface microbubble
$D_b$	Distance from bubble center to the droplet rim
$D_s$	Distance from bubble center to the droplet surface
$\nabla$	Nabra operator
$D$	Hydrogen diffusion coefficient in surface droplets
$C_w(D_s)$	Local water concentration with the distance $D_s$ from the droplet surface
$C_w(D_s) _{D_s=0}$	Theoretical water concentration nearing the droplet surface
$C_{SiH}$	Water concentration in the droplet
$k_r$	Reaction rate constant
$\epsilon$	Characteristic diffusion length of water in surface droplets
$\dot{m}(D_s)$	Local production rate of hydrogen by the chemical reaction
$\dot{m}(D_s) _{D_s=0}$	Theoretical production rate of hydrogen nearing the droplet surface
$\dot{r}(D_s)$	Local average growth rate of hydrogen bubbles
$\dot{r}(D_s) _{D_s=0}$	Theoretical average growth rate of hydrogen bubbles nearing the droplet surface

## Acknowledgement

XHZ acknowledges Future Energy Systems (Canada First Research Excellence Fund), the start-up fund from Faculty of Engineering, University of Alberta, the Canada Research Chairs program, the Canada Foundation for Innovation (CFI) and Alberta-innovates. The work is partly supported by the funding support from the Natural Science and Engineering Research Council of Canada (NSERC).

## Supporting Information Available

## References

- (1) Meng, Z.; Zhang, M.; Yang, H. Pickering emulsion droplets hosting ionic liquid catalysts for continuous-flow cyanosilylation reaction. *Green Chemistry* **2019**, *21*, 627–633.
- (2) Kim, J. B.; Lee, S. Y.; Min, N. G.; Lee, S. Y.; Kim, S.-H. Plasmonic janus microspheres created from pickering emulsion drops. *Advanced Materials* **2020**, *32*, 2001384.
- (3) Wei, Z.; Li, M.; Zeng, H.; Zhang, X. Integrated nanoextraction and colorimetric reactions in surface nanodroplets for combinative analysis. *Analytical Chemistry* **2020**, *92*, 12442–12450.
- (4) Gutierrez, J. M. P.; Hinkley, T.; Taylor, J. W.; Yanev, K.; Cronin, L. Evolution of oil droplets in a chemorobotic platform. *Nature Communications* **2014**, *5*, 5571.
- (5) Nakayama, S.; Kojima, T.; Kaburagi, M.; Kikuchi, T.; Asakura, K.; Banno, T. Chemotaxis of oil droplets and their phase transition to aggregates with membrane structures in surfactant solution containing metal salts. *ChemSystemsChem* e2100035.
- (6) Fan, X.; Sun, M.; Sun, L.; Xie, H. Ferrofluid droplets as liquid microrobots with multiple deformabilities. *Advanced Functional Materials* **2020**, *30*, 2000138.

- (7) Vannoy, K. J.; Lee, I.; Sode, K.; Dick, J. E. Electrochemical quantification of accelerated FADGDH rates in aqueous nanodroplets. *Proceedings of the National Academy of Sciences* **2021**, *118*.
- (8) Banerjee, S.; Zare, R. N. Syntheses of isoquinoline and substituted quinolines in charged microdroplets. *Angewandte Chemie* **2015**, *127*, 15008–15012.
- (9) Bain, R. M.; Pulliam, C. J.; Cooks, R. G. Accelerated Hantzsch electro spray synthesis with temporal control of reaction intermediates. *Chemical Science* **2015**, *6*, 397–401.
- (10) Yang, H.; Fu, L.; Wei, L.; Liang, J.; Binks, B. P. Compartmentalization of incompatible reagents within pickering emulsion droplets for one-pot cascade reactions. *Journal of the American Chemical Society* **2015**, *137*, 1362–1371.
- (11) Zhang, M.; Wei, L.; Chen, H.; Du, Z.; Binks, B. P.; Yang, H. Compartmentalized droplets for continuous flow liquid–liquid interface catalysis. *Journal of the American Chemical Society* **2016**, *138*, 10173–10183.
- (12) Zheng, B.; Jin, X.; Liu, J.; Cheng, H. Accelerated metal-free hydration of alkynes within milliseconds in microdroplets. *ACS Sustainable Chemistry & Engineering* **2021**, *9*, 4383–4390.
- (13) Rovelli, G.; Jacobs, M. I.; Willis, M. D.; Rapf, R. J.; Prophet, A. M.; Wilson, K. R. A critical analysis of electro spray techniques for the determination of accelerated rates and mechanisms of chemical reactions in droplets. *Chem. Sci.* **2020**, *11*, 13026–13043.
- (14) Nam, I.; Lee, J. K.; Nam, H. G.; Zare, R. N. Abiotic production of sugar phosphates and uridine ribonucleoside in aqueous microdroplets. *Proceedings of the National Academy of Sciences* **2017**, *114*, 12396–12400.
- (15) Nam, I.; Nam, H. G.; Zare, R. N. Abiotic synthesis of purine and pyrimidine ribonu-

- cleosides in aqueous microdroplets. *Proceedings of the National Academy of Sciences* **2018**, *115*, 36–40.
- (16) Nakatani, K.; Suto, T.; Wakabayashi, M.; Kim, H.-B.; Kitamura, N. Direct analyses of an electrochemically induced dye formation reaction across a single-microdroplet/water interface. *The Journal of Physical Chemistry* **1995**, *99*, 4745–4749.
- (17) Nakatani, K.; Chikama, K.; Kim, H.-B.; Kitamura, N. Droplet-size dependence of the electron transfer rate across the single-microdroplet/water interface. *Chemical Physics Letters* **1995**, *237*, 133–136.
- (18) Nakatani, K.; Wakabayashi, M.; Chikama, K.; Kitamura, N. Electrochemical studies on mass transfer of ferrocene derivatives across a single-nitrobenzene-microdroplet/water interface. *The Journal of Physical Chemistry* **1996**, *100*, 6749–6754.
- (19) Chamberlayne, C. F.; Zare, R. N. Microdroplets can act as electrochemical cells. *The Journal of Chemical Physics* **2022**,
- (20) Zhong, X.; Chen, H.; Zare, R. N. Ultrafast enzymatic digestion of proteins by microdroplet mass spectrometry. *Nature communications* **2020**, *11*, 1–9.
- (21) Burris, B. J.; Badu-Tawiah, A. K. Enzyme-catalyzed hydrolysis of lipids in immiscible microdroplets studied by contained-electrospray ionization. *Analytical Chemistry* **2021**, *93*, 13001–13007.
- (22) Huang, K.-H.; Wei, Z.; Cooks, R. G. Accelerated reactions of amines with carbon dioxide driven by superacid at the microdroplet interface. *Chemical Science* **2021**, *12*, 2242–2250.
- (23) Lee, J. K.; Han, H. S.; Chaikasetin, S.; Marron, D. P.; Waymouth, R. M.; Prinz, F. B.; Zare, R. N. Condensing water vapor to droplets generates hydrogen peroxide. *Proceedings of the National Academy of Sciences* **2020**, *117*, 30934–30941.

- (24) Lee, J. K.; Kim, S.; Nam, H. G.; Zare, R. N. Microdroplet fusion mass spectrometry for fast reaction kinetics. *Proceedings of the National Academy of Sciences* **2015**, *112*, 3898–3903.
- (25) Ju, Y.; Zhang, H.; Wang, W.; Liu, Q.; Yu, K.; Kan, G.; Liu, L.; Jiang, J. Aqueous-microdroplet-driven abiotic synthesis of ribonucleotides. *The Journal of Physical Chemistry Letters* **2022**, *13*, 567–573.
- (26) Fallah-Araghi, A.; Meguellati, K.; Baret, J.-C.; El Harrak, A.; Mangeat, T.; Karplus, M.; Ladame, S.; Marques, C. M.; Griffiths, A. D. Enhanced chemical synthesis at soft interfaces: A universal reaction-adsorption mechanism in microcompartments. *Physical Review Letters* **2014**, *112*, 028301.
- (27) Li, Z.; Kiyama, A.; Zeng, H.; Lohse, D.; Zhang, X. Speeding up biphasic reactions with surface nanodroplets. *Lab on a Chip* **2020**, *20*, 2965–2974.
- (28) Li, Z.; Kiyama, A.; Zeng, H.; Zhang, X. Size effect on the reaction rate of surface nanodroplets. *The Journal of Physical Chemistry C* **2021**, *125*, 15324–15334.
- (29) Lohse, D.; Zhang, X., et al. Surface nanobubbles and nanodroplets. *Reviews of Modern Physics* **2015**, *87*, 981.
- (30) Bao, L.; Rezk, A. R.; Yeo, L. Y.; Zhang, X. Highly ordered arrays of femtoliter surface droplets. *Small* **2015**, *11*, 4850–4855.
- (31) Feng, W.; Ueda, E.; Levkin, P. A. Droplet microarrays: from surface patterning to high-throughput applications. *Advanced Materials* **2018**, *30*, 1706111.
- (32) Zhou, L.; Yang, S.; Quan, N.; Geng, Z.; Wang, S.; Zhao, B.; Wang, X.; Dong, Y.; Tai, R.; Hu, J.; Zhang, L. Wetting behavior of surface nanodroplets regulated by periodic nanostructured surfaces. *ACS Applied Materials & Interfaces* **2021**, *13*, 55726–55734.

- (33) Zhang, X.; Lu, Z.; Tan, H.; Bao, L.; He, Y.; Sun, C.; Lohse, D. Formation of surface nanodroplets under controlled flow conditions. *Proceedings of the National Academy of Sciences* **2015**, *112*, 9253–9257.
- (34) Qian, J.; Arends, G. F.; Zhang, X. Surface nanodroplets: formation, dissolution, and applications. *Langmuir* **2019**, *35*, 12583–12596.
- (35) Bao, L.; Werbiuk, Z.; Lohse, D.; Zhang, X. Controlling the growth modes of femtoliter sessile droplets nucleating on chemically patterned surfaces. *The Journal of Physical Chemistry Letters* **2016**, *7*, 1055–1059.
- (36) Dyett, B. P.; Zhang, X. Accelerated formation of H<sub>2</sub> nanobubbles from a surface nanodroplet reaction. *ACS nano* **2020**, *14*, 10944–10953.
- (37) Ramiasa, M.; Ralston, J.; Fetzer, R.; Sedev, R.; Fopp-Spori, D. M.; Morhard, C.; Pacholski, C.; Spatz, J. P. Contact line motion on nanorough surfaces: A thermally activated process. *Journal of the American Chemical Society* **2013**, *135*, 7159–7171.
- (38) Lessel, M.; Bäumchen, O.; Klos, M.; Hähl, H.; Fetzer, R.; Paulus, M.; Seemann, R.; Jacobs, K. Self-assembled silane monolayers: an efficient step-by-step recipe for high-quality, low energy surfaces. *Surface and Interface Analysis* **2015**, *47*, 557–564.
- (39) Asenath Smith, E.; Chen, W. How to prevent the loss of surface functionality derived from aminosilanes. *Langmuir* **2008**, *24*, 12405–12409.
- (40) Li, M.; Bao, L.; Yu, H.; Zhang, X. Formation of multicomponent surface nanodroplets by solvent exchange. *The Journal of Physical Chemistry C* **2018**, *122*, 8647–8654.
- (41) Lu, Z.; Peng, S.; Zhang, X. Influence of solution composition on the formation of surface nanodroplets by solvent exchange. *Langmuir* **2016**, *32*, 1700–1706.

- (42) Lv, P.; Peñas, P.; Le The, H.; Eijkel, J.; van den Berg, A.; Zhang, X.; Lohse, D. Self-propelled detachment upon coalescence of surface bubbles. *Phys. Rev. Lett.* **2021**, *127*, 235501.
- (43) Wei, Z.; You, J. B.; Zeng, H.; Zhang, X. Interfacial partitioning enhances microextraction by multicomponent nanodroplets. *The Journal of Physical Chemistry C* **2022**, *126*, 1326–1336.
- (44) Wang, H.; Wei, Z.; Vagin, S. I.; Zhang, X.; Rieger, B.; Meldrum, A. Ultrasensitive picomolar detection of aqueous acids in microscale fluorescent droplets. *ACS Sensors* **2022**, *7*, 245–252.
- (45) Vega-Sánchez, C.; Peppou-Chapman, S.; Zhu, L.; Neto, C. Nanobubbles explain the large slip observed on lubricant-infused surfaces. *Nature Communications* **2022**, *13*, 351.
- (46) Zhang, X.; Lohse, D. Perspectives on surface nanobubbles. *Biomicrofluidics* **2014**, *8*, 041301.
- (47) Abou-Saleh, R. H.; Armistead, F. J.; Batchelor, D. V.; Johnson, B. R.; Peyman, S. A.; Evans, S. D. Horizon: microfluidic platform for the production of therapeutic microbubbles and nanobubbles. *Review of Scientific Instruments* **2021**, *92*, 074105.
- (48) Fayyaz, M.; Jabeen, M.; Tsipursky, M. S.; Irudayaraj, J. Dextran-based oxygen nanobubbles for treating inner retinal hypoxia. *ACS Applied Nano Materials* **2021**, *4*, 6583–6593.

# Graphical TOC Entry

